

Positron annihilation spectroscopy guided by two-component density functional theory calculations distinguishes irradiation-induced vacancy type in 4H-SiC

Cite as: J. Appl. Phys. 136, 145905 (2024); doi: 10.1063/5.0226531

Submitted: 2 July 2024 · Accepted: 30 September 2024 ·

Published Online: 14 October 2024



Jian Li,^{1,2} Jianrong Sun,^{1,2,a)} Yinan Tian,^{1,2} Wei Zhang,^{1,2} Hailong Chang,^{1,2} and Pengcheng Gao^{1,2}

AFFILIATIONS

¹Institute of Modern Physics, Chinese Academy of Sciences, Lanzhou 730000, China

²School of Nuclear Science and Technology, University of Chinese Academy of Sciences, Beijing 100049, China

^{a)}Author to whom correspondence should be addressed: sunjr@impcas.ac.cn

ABSTRACT

Based on two-component density functional theory integrated with the projector augmented-wave basis and incorporating both calculated and experimental data from Positron Annihilation Spectroscopy (PAS), this study introduces a novel method for identifying and analyzing specific types of vacancies when multiple types of vacancies are coexisting. This method was then tested on 4H-SiC irradiated by 300 keV C^{4+} ion beams. By calculating charge density to analyze positron annihilation lifetime spectroscopy and calculating wave functions to analyze slow positron-beam Doppler broadening spectroscopy, for the first time, silicon monovacancies (V_{Si}) and carbon monovacancies (V_C) in irradiated 4H-SiC were quantitatively detected separately, allowing them to be distinguished with high accuracy. In addition, a decreasing trend in the relative percentage of V_C with increasing irradiation dose, consistent with that expected when irradiating with carbon ions, was also observed, illustrating both the effectiveness and potential of this method for broader applications in material defect analysis. This study not only addresses the challenges of identifying multiple coexisting vacancy types using PAS but also extends the applicability and depth of PAS in fields such as nuclear energy, aerospace, and semiconductors.

© 2024 Author(s). All article content, except where otherwise noted, is licensed under a Creative Commons Attribution-NonCommercial-NoDerivs 4.0 International (CC BY-NC-ND) license (<https://creativecommons.org/licenses/by-nc-nd/4.0/>). <https://doi.org/10.1063/5.0226531>

I. INTRODUCTION

Radiation is ubiquitous and causes atoms in crystalline materials to leave their lattice positions, resulting in various types of damage and affecting material properties^{1,2} and may have a complex combination of effects on other properties of the material.^{3,4} Schottky defects and Frenkel pairs, both point defects with numerous vacancies, are typical forms of damage. Silicon carbide (SiC), a strong ceramic and wide-bandgap semiconductor, has excellent thermal, mechanical, and electromagnetic properties, along with irradiation resistance. Thus, SiC is widely used as a structural material in nuclear and space environments and is a significant third-generation semiconductor material. However, defects can be introduced in SiC crystals due to prolonged neutron and ion irradiation in these environments and also during doping processes in semiconductor production.

In particular, vacancies with high migration energies tend to remain immobile,⁵ leading to long-term retention. These vacancies can alter the semiconductor band structure,⁶ hinder charge carrier mobility,⁶ induce local internal stress, and participate in helium bubble formation, adversely affecting the material's thermal, mechanical, and electromagnetic properties. Therefore, accurately detecting and understanding vacancy defects caused by neutron and ion irradiation is essential for the reliable application of SiC.

Positron Annihilation Spectroscopy (PAS) is a highly sensitive, non-destructive technique for examining vacancy-type defects⁷ in crystalline materials. It employs two primary methods: Positron Annihilation Lifetime Spectroscopy (PALS) and Slow Positron-beam Doppler Broadening Spectroscopy (SPDBS). PALS can identify different types of vacancies by comparing experimentally determined positron lifetimes with theoretical calculations.

19 October 2024 05:05:10

However, the accuracy of vacancy-type identification relies heavily on precise positron lifetime calculations, particularly in silicon carbide (SiC). Previous studies on SiC have inconsistently attributed positron lifetimes ranging from 170 to 210 ps to silicon monovacancies (V_{Si}), while considering lifetimes for carbon monovacancies (V_{C}) indistinguishable from vacancy-free crystals.^{8–10}

SPDBS, another commonly used PAS technique, analyzes two line shape parameters, S and W , to determine positron annihilation mechanisms.¹¹ However, distinguishing multiple types of vacancies using traditional SPDBS analysis is challenging. In SiC, previous studies^{10,12} using S – W analysis have identified the presence of vacancy-type defects but could not specifically distinguish between various coexisting vacancies.

There are several reasons for these difficulties and challenges. For PALS, early Density Functional Theory (DFT) calculations of positron lifetimes in vacancy sites used approximations that ignored the influence of positron presence on the relaxation of surrounding atoms.^{9,13} The positron lifetime in a vacancy site is highly sensitive to the vacancy's free-space volume, and this approximation could significantly affect the accuracy of the results. For SPDBS, the experimental data include contributions from all types of vacancies, but the calculation windows for line shape parameters such as S and W are mostly chosen empirically. This empirical selection prevents these parameters from accurately representing contributions from each specific type of vacancy.

To address these difficulties and challenges, this study proposes a comprehensive analysis method that combines accurate theoretical calculations with experiments.

II. METHODOLOGY

A. Theoretical calculation

For the *ab initio* calculations of positron annihilation, we use Two-Component Density Functional Theory (TC-DFT)^{14–17} to fix the wavefunctions of electrons and positrons as background and self-consistently calculate each other's wavefunctions, respectively, until both electronic and positronic components converge. In each cycle, atomic forces and movements were simultaneously computed via ABINIT^{18,19} code to account for the interaction between positrons and electrons, ensuring the correct simulation of vacancy structure changes in the presence of positrons.^{20,21} We also calculated the SPDBS by preparing a customized Projector Augmented-Wave (PAW)²² basis and obtained accurate theoretical data in both low- and high-momentum regions, which enabled us to accurately distinguish different types of vacancies using SPDBS. This special PAW basis was generated using the ATOMPAW²³ code and includes silicon atom $2s^2 2p^6$ electrons to achieve higher completeness than ordinary pseudopotentials by accurately modeling the inner-shell electrons with higher momentum. It is noteworthy that despite the introduction of an updated generalized gradient approximation (GGA) electron–positron correlation functional, this study employs the local-density approximation (LDA). Previous research has demonstrated that LDA provides a superior Doppler ratio spectrum compared to GGA,²⁴ which is crucial for distinguishing vacancy types in this study. Recently, Makkonen and Tuomisto²⁵ utilized both calculated and experimental Doppler ratio spectra to reveal significantly different line shapes

between Ga vacancies and Be_{Ga} antisites in GaN:Be. They also identified weak positron trapping from more general Rydberg states even if they have no open volume, further highlighting the potential of accurate Doppler ratio spectra in characterizing specific types of defects, especially if those insights could be incorporated with the statistical parameter scheme we proposed in this study.

The computational model used in this study consists of a 4H-SiC $3 \times 3 \times 3$ supercell containing 216 atoms. The initial state of the vacancy-type defects is constructed by removing atoms near the center of the supercell in real space, serving as the starting point for calculations. In each self-consistent field (SCF) cycle, each atom is allowed to relax its position according to the forces acting upon it, utilizing the Limited-memory Broyden–Fletcher–Goldfarb–Shanno (L-BFGS) algorithm. The relaxation continues until the maximum atomic force is below 50 meV/Å, with the convergence criterion of 5 meV/Å for each SCF cycle, and the energy cutoff is set at 25 hartree. Through rigorous testing, this set of parameters leads to the convergence of both the total energy and the positron lifetime. The SCF cycle for electrons and positrons uses two k -points for sampling: one at the Γ -point and the other at the boundary of the Brillouin zone. The calculation of the positron annihilation momentum distribution spectrum uses the Γ -point only.

In this study, two types of positron spectroscopy values are used: the positron lifetime in vacancies, denoted as τ , and the momentum distribution of positron annihilation, denoted as $\rho(\mathbf{p})$. For the positron lifetime τ , an integral over the entire space of the product of positron and electron densities [denoted as $\rho_e(\mathbf{r})$ and $\rho_p(\mathbf{r})$, respectively] is acquired using ABINIT code, along with an electron–positron-dependent enhancement factor²⁶ $g(e, p)$ based on the work of Boronski and Nieminen,¹⁵ to compute the positron annihilation rate λ using the following equation:¹⁷

$$\lambda = \pi r_e^2 c \int d\mathbf{r} \rho_e(\mathbf{r}) \rho_p(\mathbf{r}) g(e, p), \quad (1)$$

where r_e is the classical electron radius and c is the speed of light. The reciprocal of λ then directly yields the theoretical positron lifetime as $\tau = 1/\lambda$.

The calculation of theoretical momentum distribution $\rho(\mathbf{p})$ of positron annihilation involves summing all integrations over the real space of the product of momentum-dependent electron and positron wavefunctions (denoted as Ψ_e and Ψ_p , respectively) is needed,¹⁷ as depicted in the following equation:

$$\rho(\mathbf{p}) = \pi r_e^2 c \sum_j \gamma_j \left(\int d\mathbf{r} e^{-i\mathbf{p} \cdot \mathbf{r}} \Psi_{e,j}(\mathbf{r}) \Psi_{p,j}(\mathbf{r}) \right)^2, \quad (2)$$

where $\gamma_j = \lambda_j / \lambda_{j,\text{IPM}}$ is an enhancement factor²⁷ for state j , and λ_j and $\lambda_{j,\text{IPM}}$ are both the positron annihilation rate in state j , calculated with the aforementioned electron–positron-dependent factor $g(e, p)$ and independent particle model (IPM), respectively.

It is important to note that there are still multiple limitations and uncertainties in the computational framework described above. First, the band structure of semiconductors results in a more complex and inhomogeneous screening effect of electrons on nuclei near crystal defects. However, the enhancement factor used in current theoretical calculations to incorporate this effect remains relatively simple, which may lead to inaccurate results. Second, in

experiments, determining the momentum's direction is often difficult. Consequently, theoretical calculations typically perform one-dimensional momentum density calculations for each of the three crystal directions, and the average of these three one-dimensional spectra is used as the theoretical spectrum. This approximation can introduce new errors in the construction of statistical parameters for crystals with high structural anisotropy. Additionally, the completeness of the PAW basis significantly affects the accuracy of the Doppler momentum spectrum. Thus, the precise construction of a PAW basis is crucial for accurately distinguishing vacancy types. For non-crystalline materials, there is still a need to develop accurate, quantitative theoretical models in order to correctly interpret experimental data.²⁸

B. Materials and ion irradiation

The sample is an n-type doped monocrystalline 4H-SiC wafer produced by Hefei Kejing Materials Technology Co., Ltd. The wafer has a hexagonal wurtzite phase with surface crystallographic orientation $\langle 0001 \rangle$ and has been cut into sheets of $10 \times 10 \times 0.33$ mm. The surface is treated with chemical mechanical polishing, with a surface roughness of $R_a \leq 15$ Å and the silicon atomic surface is defined as the frontal face for the incoming radiation beam. A total of 10 sheets were divided into five sets, two sheets per set, four of which were then used for irradiation experiments.

The irradiation experiments were performed on the 320 kV multi-discipline research platform equipped with an electron cyclotron resonance (ECR) ion source at the Institute of Modern Physics, Chinese Academy of Sciences (IMP, CAS). We irradiated four sets of 4H-SiC single-crystal samples with dose ranges 10^{13} – 10^{16} cm⁻² and dose rates 3×10^{11} cm⁻² s⁻¹ using 300 keV C⁴⁺ ions at room temperature (293 K) in a vacuum (below 1×10^{-6} Pa) to introduce various types of vacancies. The experiment used a low irradiation dose rate and a water-cooling system behind the sample/target holder to ensure that the irradiation temperature was RT. In addition, the low dose rate ensured that interference between different incident ions was minimized and allowed the low-dose (10^{13} – 10^{14} cm⁻²) groups to produce predominantly monovacancies. The high-dose (10^{15} – 10^{16} cm⁻²) group produces divacancies and vacancy clusters with a larger average size. One additional set of unirradiated 4H-SiC single crystals served as a control set.

C. Positron annihilation lifetime spectroscopy (PALS)

PALS measurements were carried out at the Institute of High Energy Physics, Chinese Academy of Sciences (IHEP, CAS), using a ²²Na positron source with a radioactivity of 13 μCi. Two 4H-SiC samples to be tested are placed in close contact with the positron source on either side, forming a standard “sandwich” configuration, and then subjected to spectroscopic measurements. A pair of BaF₂ scintillator detectors are used to detect the gamma photons released after positron annihilation, and the measurement of the positron annihilation lifetime spectra is realized by the fast-slow coincidence measurement technique, with a total count of 2×10^6 for each set of lifetime spectra. The time resolution of the spectrometer is 210 ps, and the electronic plug-in of the measurement system is the standard NIM plug-in of EG&G.

D. Slow positron-beam Doppler broadening spectroscopy (SPDBS)

SPDBS measurements were carried out at the ²²Na slow positron beam line at the Institute of High Energy Physics, Chinese Academy of Sciences (IHEP, CAS). A high-purity germanium detector array was used to measure the momentum of gamma photons released after positron annihilation. The spot of the slow positron beam is 6 mm wide, significantly smaller than the 10 mm sample size to ensure that measurements are free of boundary interferences. The energy range of the slow positron beam is between 0.5 and 25 keV, with a step size of 0.5 keV in the range of 0.5–5 keV and 1 keV in the range of 5–25 keV.

III. RESULTS AND DISCUSSION

Following the irradiation experiments, the analysis of PALS and SPDBS results provided pivotal insights. The PALS data, when analyzed using PALSfit3 software,²⁹ and compared to theoretical lifetimes obtained with TC-DFT calculation, enable us to distinguish silicon monovacancies (V_{Si}) from carbon monovacancies (V_C), and it also shows different trends of their concentrations with increasing irradiation dose. When the SPDBS data combined with TC-DFT calculations are used to construct our proposed “P” parameter, it is possible to use this parameter to directly differentiate between V_{Si} and V_C and to obtain different trends of their concentrations with increasing irradiation dose. This differentiation not only bridges the gap between theoretical predictions and empirical data but also sets the stage for detailed comparisons of samples being irradiated with various doses, further elaborated in Secs. III A and III B.

A. PALS measurements and vacancy-type distinguishment

Figure 1(a) shows the raw PALS data, including data measured from the unirradiated control set vs four sets of samples after irradiation with doses ranging from 10^{13} – 10^{16} cm⁻². The channel with the highest data counts for each set was defined as channel 0 and aligned at channel 0. All counts were normalized and added fixed offset for visual distinguishment and comparison. Figure 1(b) shows the lifetime components extracted from raw data using PALSfit3 software,²⁹ using a fitting method with unrestrained numbers of components to minimize arbitrariness. The component τ_0 is obtained from unirradiated samples, and its corresponding counts are deducted as background in other irradiated spectra to amplify irradiation-induced components τ_1 and τ_2 . Figure 1(c) shows the relative intensities of lifetime components τ_1 and τ_2 in the total lifetime spectrum, marked as I_1 and I_2 . It is worth noting that since the theoretical calculations expect relatively close values of positron lifetimes in V_{Si} and V_C (the difference between the two is ~40 ps), which is close to the limit of what can be resolved by the instrument we are using, to ensure that the fits are valid, we performed multiple background subtractions. We first performed the standard two-component fitting for all spectra to obtain a lattice component and a defect component, along with their intensities. Then, in addition to the standard subtraction of the constant background and the source term, we take the entire lifetime spectra of the unirradiated sample, multiply it with the

19 October 2024 05:05:10

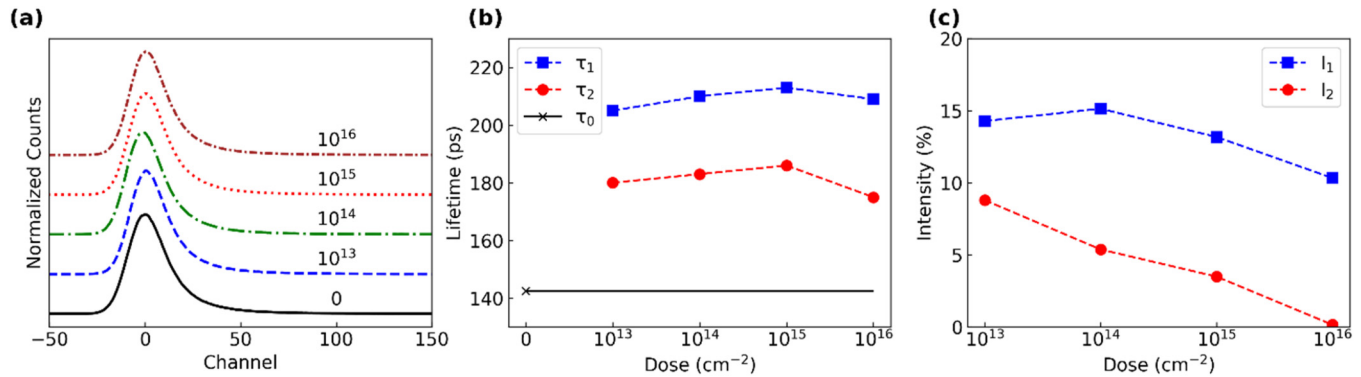


FIG. 1. (a) Original experimental PALS data include the unirradiated sample and four irradiated samples at different doses. (b) Three positron lifetime components, τ_0 , τ_1 , and τ_2 , were obtained by fitting the original experimental PALS data through using our TC-DFT calculated values as the fitting reference. Here, τ_0 corresponds to the positron lifetime in the unirradiated sample, and τ_1 and τ_2 correspond to positron lifetimes in the two types of vacancies in irradiated samples, respectively. (c) I_1 and I_2 correspond to the intensities of the aforementioned lifetime components τ_1 and τ_2 , respectively.

lattice component intensity in all irradiated samples, using the result as a special “background,” and subtract it from the lifetime spectra of all irradiated samples, to further amplify the lifetime components corresponding to the expected irradiation-induced vacancies. A second round of two-component fitting was then performed on these amplified spectra, and the two different vacancy components shown in Figs. 1(b) and 1(c) were obtained.

Table I lists the calculated positron annihilation lifetimes for both defect-free 4H-SiC crystals and eight types of vacancies, including four types of monovacancies (Si or C monovacancies located on *h* or *k* site), three types of divacancies (the absence of two Si atoms, two C atoms, or one Si atom and one C atom), and a three-vacancy cluster (the absence of three Si atoms), using the calculation method mentioned above.

By comparing Fig. 1(b) with Table I, the experimentally measured lifetime component τ_0 (~142 ps) is closest to the theoretically calculated no vacancy lifetime (145 ps); the experimental lifetime component τ_1 (~210 ps) is closest to the theoretically calculated V_{Si} lifetime (216~218 ps); and the experimental lifetime component τ_2 (~181 ps) is closest to the theoretically calculated V_C lifetime (170~178 ps). Larger vacancy clusters have theoretical lifetimes that deviate much more from these experimental lifetime components, and they should not be presented in lower dose (10^{13} – 10^{14} cm⁻²) samples based on the SPDBS results in Fig. 2(b). Therefore, we can conclude that the three lifetime components τ_0 , τ_1 , and τ_2 signal the annihilation of positrons in the vacancy-free part of 4H-SiC, in V_{Si} and V_C . The results are comparable to the positron lifetime values in similar vacancies in ion-irradiated 6H-SiC reported in previous studies,^{30,31} reflecting the consistency of the result of PALS in different types of hexagonal SiC.

Figure 1(c) reveals a significant reduction of I_2 with increasing irradiation dose, indicating a decrease in the abundance of V_C monovacancies. This trend is consistent with that obtained later using SPDBS and can be explained by the recombination of C ions and V_C . Since the irradiated ion we used is the carbon ion, which is one of the two elements constituting SiC and has a smaller atomic size than silicon, after it is incident on the SiC crystals and loses most of its energy, it can easily combine and stabilize with a nearby size-matched carbon monovacancy V_C , resulting in a decrease in the relative concentration of V_C in the samples when the irradiation dose is high. As a result of the simple vacancy identification given by PALS, it also agrees with the results obtained by the SPDBS-based P-parameter method that we propose in the later section, thus providing corroboration of the validity of the method.

From Fig. 1 and Table I, it becomes evident that by considering the effect of positron annihilation on the relaxation of the vacancy structure in the calculation, it is possible to obtain theoretical lifetimes that are highly consistent with the PALS experimental results, thus enabling the use of the PALS technique to distinguish between V_{Si} , V_C , and vacancy-free crystals in 4H-SiC for the first time, instead of assuming that V_C and vacancy-free crystals are indistinguishable as in the previous study.^{8–10}

B. SPDBS measurements and vacancy-type distinguishment

After successfully differentiating V_{Si} from V_C using the PALS technique, we further explored this differentiation through the SPDBS technique. Upon calculating the theoretical SPDBS for bulk SiC and various vacancy types using this method, we proceed with

TABLE I. Theoretical calculations of PALS for 4H-SiC defect-free crystals and eight vacancy-type defects.

Vacancy type	No vacancy	V_{Si}		V_C		V_{SiSi}	V_{3Si}	V_{CC}	V_{SiC}
Atomic site	...	H	k	h	K	hh	hkh	kk	hk
Theoretical lifetime (ps)	145	218	216	178	170	227	227	167	224

19 October 2024 05:05:10

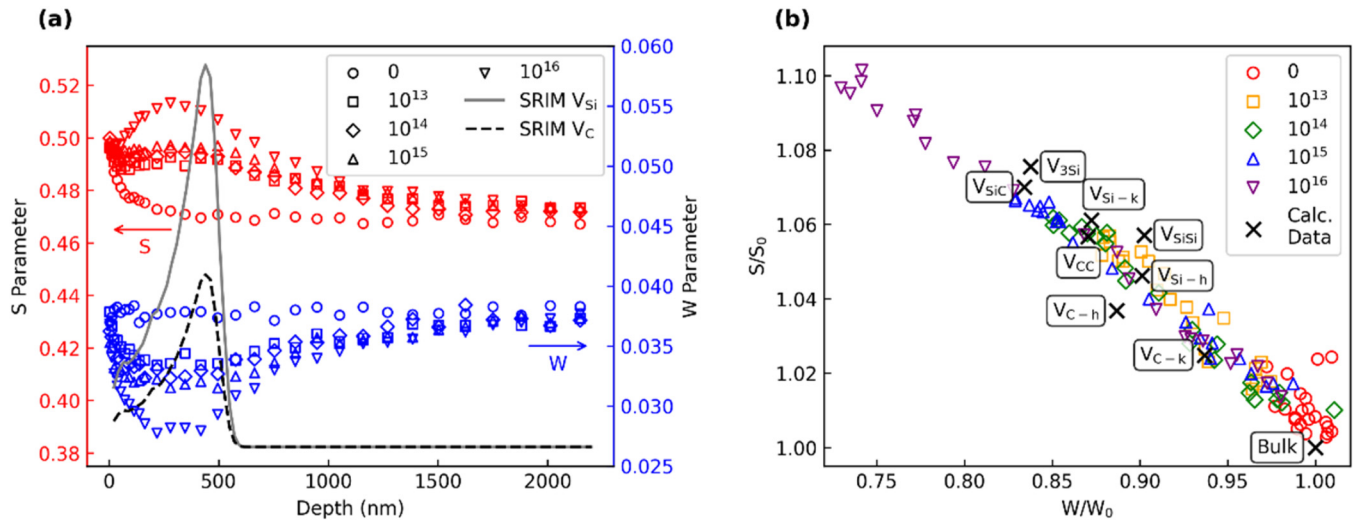


FIG. 2. (a) Depth-S/W parameter profiles for unirradiated and irradiated samples (hollow markers), and the distribution of ion-introduced vacancies along the direction of incidence depth obtained from SRIM simulations (curved lines). (b) Relative S-W plot, including experimental S-W data for unirradiated and irradiated samples (hollow markers); our TC-DFT calculated theoretical S-W data (x-shape markers), with eight points of different types of vacancies and one point of the vacancy-free bulk crystal, all labeled individually.

the conventional analysis of S-W parameters based on these theoretical and experimental SPDBS. However, each experimental SPDBS represents a total spectrum composed of contributions from multiple vacancy types at unknown ratios, complicating direct differentiation of the coexisting vacancies based solely on the theoretical SPDBS obtained through Eq. (2). To address this issue, we introduce a novel statistical analysis technique. The methodologies and results of both the conventional analysis of S-W parameters and the novel statistical analysis are described below.

In the conventional analysis scheme, each set of S-W parameters is derived from the corresponding SPDBS: the energy of gamma photons at 511.0 keV was defined as the peak position, and the peak region was defined as ± 11.5 keV around this peak. The S parameter was defined as the ratio of counts within ± 0.8 keV of the peak to the total counts in the peak region. The W parameter was defined as the ratio of counts within $\pm 2.6 \sim 5.9$ keV of the peak to the total counts in the peak region.

Figure 2(a) shows the S and W parameters of the SPDBS obtained by 0.5–25 keV slow positron beams on the samples. The x axis indicates the depth within 4H-SiC crystals, translated from the energy of the slow positron beams, and displays the S and W parameters at various depths up to 2200 nm from the irradiated surface for each group of samples. Additionally, SRIM³²-simulated distribution-depth curves of V_{Si} and V_C in SiC crystals caused by 300 keV C^{4+} ion irradiation are shown in this figure with the solid and dashed lines, respectively.

From Fig. 2(a), it can be observed that beyond a shallow surface region (depth <100 nm), the S and W parameters of all sample groups predominantly vary within a depth of no more than 700 nm. Beyond 1400 nm in depth, the S and W parameters of all sample groups are no longer affected by the radiation dose. In

SPDBS, the S and W parameters are closely associated with vacancy concentration, suggesting that irradiation-induced vacancies are mainly concentrated within a depth of up to 700 nm from the surface. Regions deeper than 1400 nm appear free from vacancies detectable by SPDBS, and shallow vacancies no longer influence positron annihilation in these deeper regions. This depth range is consistent with the SRIM simulation.

In addition to the traditional S-W analysis, Fig. 2(b) illustrates the relationship between S and W parameters and compares experimental data for all samples (hollow markers with dosage color code) with calculated data for eight types of vacancies (cross markers with vacancy name tags). These parameters are shown in their relative forms, S/S_0 and W/W_0 , where S_0 and W_0 are the average S and W parameters measured at depths beyond 1400 nm for each sample, respectively. All data points align along a common slope in the S-W plot, indicating a consistent positron annihilation mechanism across samples, primarily involving various vacancy defects. For calculated data, as the vacancy size increases from monovacancies to larger clusters, W/W_0 decreases, while S/S_0 increases. Experimental data show a similar inverse correlation between W/W_0 and S/S_0 as the irradiation dose increases from 0 to 10^{16} cm^{-2} . During annihilation, a stationary positron-electron pair produces two photons, each with an energy of 511.0 keV, emitted in opposite directions at an angle of 180° . The initial kinetic energy of the electron can cause deviations in photon energy relative to their scattering angle. The S parameter quantifies the concentration of annihilation photons around the 511.0 keV peak, while the W parameter measures photons with higher energy deviations at wider scattering angles. Increasing radiation dose leads to higher S/S_0 and lower W/W_0 , suggesting that positrons are less likely to annihilate with inner-shell high-energy electrons in highly

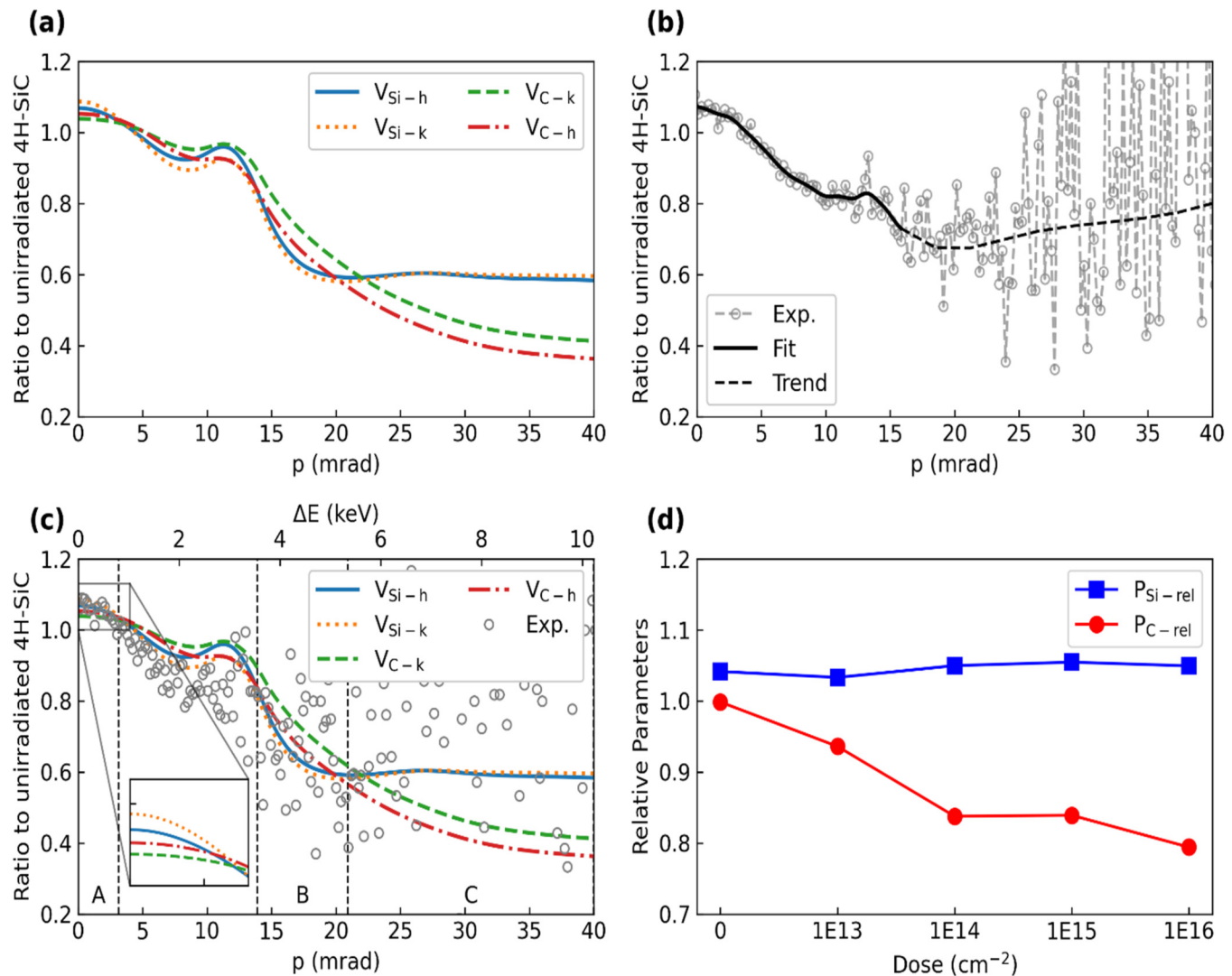
19 October 2024 05:05:10

irradiated samples. This implies that the vacancy size and type produced at different irradiation doses can be inferred from the $S/S_0-W/W_0$ relationship in experimental SPDBS data, compared to theoretical values for various vacancies. At low irradiation doses (10^{13} – 10^{14} cm $^{-2}$), monovacancies predominate, whereas higher doses (10^{15} – 10^{16} cm $^{-2}$) lead to the appearance of divacancies and larger clusters. Lower irradiation doses result in experimental data points closer to the lower right corner of the $S/S_0-W/W_0$ plot, indicating a higher percentage of monovacancies.

Although the $S/S_0-W/W_0$ analysis of the SPDBS described above can provide insights into the variations of vacancy size in the

sample with irradiation dose, it is still unable to directly differentiate the two basic types of monovacancies, V_{Si} and V_C , much less to determine which one is more numerous. To address this, we aligned the theoretical SPDBS of various vacancy types, calculated as mentioned earlier, with the theoretical SPDBS peaks of the undamaged crystal at 511.0 keV. We then obtained the ratio spectra of these vacancy types based on them, using the energy deviated from 511.0 keV as the x axis. This resulted in the SPDBS ratio plot as depicted in Fig. 3.

Figure 3(a) shows the calculated SPDBS ratio spectrum of five types of vacancies (marked by dotted and dashed lines). The x axis



19 October 2024 05:05:10

FIG. 3. (a) The calculated theoretical SPDBS ratio plot of four different types of vacancies. (b) The experimental SPDBS ratio data of the irradiated sample with 10^{15} cm $^{-2}$ dose. (c) The calculated theoretical SPDBS ratio plot with experimental SPDBS ratio data of the irradiated sample with 10^{16} cm $^{-2}$ dose, and A-B-C zoning for P-parameter calculations. The zoomed-in part shows the calculated SPDBS ratio spectrum details of four different types of vacancies in the low ΔE range. (d) Variation in two relative statistical parameters, P_{Si-rel} and P_{C-rel} for all samples with different irradiation doses.

represents the scattering angle (p) of the pair of photons and the photon energy difference (ΔE) from 511.0 keV. There are four basic monovacancies, V_{Si} and V_C , each located at two different geometric positions (h and k sites), and the fifth type is a representative divacancy formed by combining V_{Si} and its closest V_C . All theoretical curves have a characteristic peak around $10 < p < 15$ mrad, as indicated by the red box marker. Figure 3(b) shows a set of experimental data (marked by gray hollow circles) measured at a depth of 350 nm in a sample irradiated with a dose of 10^{15} cm^{-2} and the solid curve fitted to the data using $\text{FWHM} = 0.1 \text{ keV}$. The experimental values also show the characteristic peak in the same range of $10 < p < 15$ mrad, as indicated by the red box marker. In the high ΔE region ($p > 16$ mrad, corresponding $\Delta E > 5 \text{ keV}$), the experimental values begin to oscillate significantly, rendering it difficult for the fitted curves (trends represented by a dashed line) in this region to be directly compared with the theoretical curves. This is because of the low absolute count rates in the high ΔE region, leading to significant local oscillations when the two sets of experimental values are divided to produce the ratio spectrum, which is an inherent deficiency of the PAS technique in acquiring data from the high ΔE region, and the P-parameter proposed in this study is designed to address it. Because the construction of the P-parameter is based on the mean of a large number of spectra, statistical fluctuations due to low count rates can be expected to be canceled out. For this reason, traditional non-coincidence spectroscopy, which is significantly faster than coincidence Doppler broadening spectroscopy, but with a lower signal-to-noise ratio, could also be employed for calculating the P-parameter to decrease costs. Figure 3(c) is a combined plot of theoretical data from (a) and experimental data measured at a depth of 350 nm in a sample irradiated with a dose of 10^{16} cm^{-2} . The calculated and experimental values match well near 511.0 keV ($\Delta E < 5 \text{ keV}$). Using the combined data in Fig. 3(c), we can define three specific regions: A ($0 < \Delta E < 0.8 \text{ keV}$), B ($3.55 < \Delta E < 5.35 \text{ keV}$), C ($\Delta E > 5.35 \text{ keV}$). In regions A and C, the theoretical values of V_{Si} (dotted line) are higher than those for V_C (dashed line), while in region B, the theoretical values for V_{Si} are lower than those of V_C .

Subsequently, we define the following expressions for statistical parameters P_{Si} and P_C , which are used to amplify the distinct features of V_{Si} and V_C in the ratio spectrum:

$$P_{Si} = \frac{a - b + c}{\text{All}}, P_C = \frac{b - c}{\text{All}}, \quad (3)$$

where a , b , and c are the total counts of experimental SPDBS in the A, B, and C regions, respectively. The denominator "All" is the sum of all counts for the entire peak area ($0 < \Delta E < 10 \text{ keV}$). By analyzing samples subjected to various energy levels of slow positron beams, we can calculate P_{Si} and P_C values for each positron energy level, corresponding to various depths in samples. From these P_{Si} and P_C values, we then construct a set of new statistics as below:

$$P_{Si\text{-rel}} = \frac{P_{Si\text{-defect}}}{P_{Si\text{-base}}}, P_{C\text{-rel}} = \frac{P_{C\text{-defect}}}{P_{C\text{-base}}}, \quad (4)$$

where $P_{Si\text{-defect}}$ and $P_{C\text{-defect}}$ are the relative statistical parameters, they are the mean values of all P_{Si} and P_C for the severely damaged

TABLE II. Values of relative statistical parameters $P_{Si\text{-rel}}$ and $P_{C\text{-rel}}$ were obtained from the SPDBS experimental data for the five sets of samples, along with their ratio $P_{Si\text{-rel}}/P_{C\text{-rel}}$.

Dose (cm^{-2})	0	10^{13}	10^{14}	10^{15}	10^{16}
$P_{Si\text{-rel}}$	1.04	1.03	1.05	1.05	1.05
$P_{C\text{-rel}}$	1.00	0.94	0.84	0.84	0.79
$P_{Si\text{-rel}}/P_{C\text{-rel}}$	1.04	1.09	1.25	1.25	1.33

region (depth $< 700 \text{ nm}$), respectively, and $P_{Si\text{-base}}$ and $P_{C\text{-base}}$ are the mean values of all P_{Si} and P_C for the undamaged base region of the crystal (depth $> 1400 \text{ nm}$), respectively. The values of dimensionless statistics $P_{Si\text{-rel}}$ and $P_{C\text{-rel}}$ are shown in Table II.

The definition of relative statistical parameters indicates that a higher $P_{X\text{-rel}}$ value signals a greater presence of the corresponding vacancy-type X in the damaged region at depths below 700 nm. Thus, based on values of $P_{Si\text{-rel}}$ and $P_{C\text{-rel}}$, for the first time, through SPDBS experiments, we effectively distinguish between the two fundamental monovacancies in 4H-SiC, V_{Si} and V_C , and demonstrate varying trends in their relative proportions with increasing irradiation doses. Additionally, it allows the identification of which vacancies predominate in the samples. As can be seen in Fig. 3(b) with Table II, V_{Si} is in the majority in all samples and becomes more dominant as the irradiation dose increases.

Additionally, we observe in Fig. 3(d) a notable decline in $P_{C\text{-rel}}$, associated with carbon vacancies, as the irradiation dose increases. At the lowest irradiation dose (10^{13} cm^{-2}), the $P_{Si\text{-rel}}/P_{C\text{-rel}}$ ratio of 1.09 is close to 1.04 for the unirradiated sample; as the irradiation dose increases to the highest (10^{16} cm^{-2}), the $P_{Si\text{-rel}}/P_{C\text{-rel}}$ ratio rises to 1.33. This pattern aligns with the trends observed for carbon vacancies in I_C , as presented in Fig. 1(b). In contrast, parameters related to V_{Si} do not exhibit this trend. This distinctive behavior appears independently in both PALS and SPDBS results and is consistent with our expectation that C ions are recombined with V_C in SiC samples. This dose-dependent variation in vacancy concentrations is not reported with other types of ion irradiation experiments conducted before this study, indicating that the two vacancy lifetime components in the PALS results, as well as the two relative statistical parameters in the SPDBS analysis results, are both correctly corresponding to the actual V_{Si} and V_C , respectively, thus further demonstrating the validity and reliability of the method proposed in this study in distinguishing vacancy types.

IV. CONCLUSION

This study presents a novel method for identifying specific vacancy-type defects using Positron Annihilation Spectroscopy (PAS) combined with Two-Component Density Functional Theory (TC-DFT). By applying this method to 4H-SiC samples irradiated with 300 keV C^{4+} ion beams, the following conclusions can be made:

1. By using fully self-consistent Two-Component Density Functional Theory (TC-DFT) and taking into account the effects of positrons in the atomic relaxation process, the theoretical positron lifetime in vacancies can be obtained with unprecedented accuracy. By analyzing the experimental Positron

Annihilation Lifetime Spectroscopy (PALS) data using the theoretical lifetimes as constraints, the corresponding lifetime components and their intensity for various types of vacancies can be obtained. When this method was applied to 4H-SiC, it successfully distinguished two of the basic types of monovacancies (V_{Si} and V_C) for the first time using PALS data only.

2. By calculating the theoretical Slow Positron-beam Doppler Broadening Spectroscopy (SPDBS) for various types of vacancies using a high-completeness Projector Augmented-Wave (PAW) basis and constructing the relative statistical parameters corresponding to the vacancies based on calculation results and experimental SPDBS data, it is possible to differentiate between the different types of vacancies by comparing the relative statistical parameters and determining which types of vacancies are in the majority. When this method was applied to 4H-SiC, it successfully distinguished two of the basic types of monovacancies (V_{Si} and V_C) for the first time using SPDBS data only.
3. In the 4H-SiC experimental examples mentioned above, a notable decrease in the proportion of carbon vacancies (V_C) is observed as the irradiation dose increases, a phenomenon attributed to the recombination effects between carbon ions and vacancies. This trend is consistent across both PALS and SPDBS results, demonstrating the validity of the above method.
4. The novel method proposed in this study not only solves the challenge faced by the PAS technique in distinguishing multiple types of coexisting vacancies but also extends the scope and depth of applications in this field.

ACKNOWLEDGMENTS

The authors thank Professor Dr. Xinzhong Cao and Dr. Peng Zhang from IHEP-CAS for their testing support and the staff of 320 kV multi-discipline research platform at IMP-CAS for their irradiation support. This work was supported by the Project of National Key Laboratory of Neutron Science and Technology (Grant No. NST20240101), the National Natural Science Foundation of China (NNSFC) (Grant No. 12075293), and the Strategic Priority Research Program of Chinese Academy of Science (Grant No. XDA0410303).

AUTHOR DECLARATIONS

Conflict of Interest

The authors have no conflicts to disclose.

Author Contributions

Jian Li: Data curation (lead); Investigation (equal); Methodology (equal); Validation (equal); Visualization (lead); Writing – original draft (lead). **Jianrong Sun:** Conceptualization (lead); Funding acquisition (lead); Project administration (lead); Resources (lead); Supervision (lead); Writing – review & editing (lead). **Yinan Tian:** Data curation (equal); Validation (equal). **Wei Zhang:** Data curation (supporting); Validation (supporting). **Hailong Chang:** Funding acquisition (supporting); Resources (supporting). **Pengcheng Gao:** Data curation (supporting); Validation (supporting).

DATA AVAILABILITY

The data that support the findings of this study are available from the corresponding author upon reasonable request.

REFERENCES

- ¹Z. Cheng, J. Sun, X. Gao, Y. Wang, J. Cui, T. Wang, and H. Chang, “Irradiation effects in high-entropy alloys and their applications,” *J. Alloys Compd.* **930**, 166768 (2023).
- ²Z. Cheng, J. Sun, D. Chen, S. Liu, J. Cui, T. Wang, H. Chang, P. Tai, Y. Tian, J. Li, L. Zhang, L. Sun, and Y. Feng, “A multi-perspective study on the evolution behavior of helium bubbles in FeCrVTi medium-entropy alloys,” *Mater. Charact.* **216**, 114252 (2024).
- ³J. Cui, J. Sun, Z. Cheng, Z. Xu, T. Wang, J. Ren, H. Chang, and P. Tai, “Effects of precipitated phase on the synergy of corrosion resistance and mechanical properties for FeCrVTi medium-entropy alloys,” *Corros. Sci.* **224**, 111508 (2023).
- ⁴Z. Cheng, J. Sun, J. Cui, D. Chen, J. Ren, T. Wang, H. Chang, P. Tai, L. Zhang, Y. Tian, Y. Wei, and J. Li, “Microstructural evolution, strengthening and high thermal conductivity mechanisms of FeCrV-based medium-entropy alloys with Laves phase precipitation formed by adding minimal Ti,” *Mater. Charact.* **200**, 112860 (2023).
- ⁵T. Suzuki, T. Yano, T. Mori, H. Miyazaki, and T. Iseki, “Neutron irradiation damage of silicon carbide,” *Fusion Technol.* **27**(3), 314–325 (1995).
- ⁶Y. Tian, R. Li, J. Li, H. Li, X. Zheng, Z. Cheng, and J. Sun, “Effects of electric polarization and defect energy levels induced by ion irradiation on the electrical behavior of 4H-SiC Schottky barrier diodes,” *J. Phys. D: Appl. Phys.* **56**(35), 355110 (2023).
- ⁷F. A. Selim, “Positron annihilation spectroscopy of defects in nuclear and irradiated materials—A review,” *Mater. Charact.* **174**, 110952 (2021).
- ⁸S. Dannefaer and D. Kerr, “Positron annihilation investigation of electron irradiation-produced defects in 6H-SiC,” *Diamond Relat. Mater.* **13**(1), 157–165 (2004).
- ⁹T. E. M. Staab, L. M. Torpo, M. J. Puska, and R. M. Nieminen, “Calculated positron annihilation parameters for defects in SiC,” *Mater. Sci. Forum* **353–356**, 533–536 (2001).
- ¹⁰Q. Xu, T. Yoshiie, and M. Okada, “Positron annihilation of vacancy-type defects in neutron-irradiated 4H-SiC,” *J. Nucl. Mater.* **386–388**, 169–172 (2009).
- ¹¹M. Clement, J. M. M. De Nijs, P. Balk, H. Schut, and A. Van Veen, “Analysis of positron beam data by the combined use of the shape- and wing-parameters,” *J. Appl. Phys.* **79**(12), 9029–9036 (1996).
- ¹²F. Linez, “Propriété des défauts lacunaires dans le carbure de silicium : évolution de leur nature en fonction des conditions d’irradiation et interaction avec l’hélium,” Doctoral dissertation (Université d’Orléans, 2012), Français. (NNT: 2012ORLE2006).
- ¹³G. Brauer, W. Anwand, P. G. Coleman, A. P. Knights, F. Plazaola, Y. Pacaud, W. Skorupa, J. Störmer, and P. Willutzki, “Positron studies of defects in ion-implanted SiC,” *Phys. Rev. B* **54**(5), 3084–3092 (1996).
- ¹⁴R. M. Nieminen, E. Boronski, and L. J. Lantto, “Two-component density-functional theory: Application to positron states,” *Phys. Rev. B* **32**(2), 1377–1379 (1985).
- ¹⁵E. Boroński and R. M. Nieminen, “Electron-positron density-functional theory,” *Phys. Rev. B* **34**(6), 3820–3831 (1986).
- ¹⁶M. J. Puska and R. M. Nieminen, “Theory of positrons in solids and on solid surfaces,” *Rev. Mod. Phys.* **66**(3), 841–897 (1994).
- ¹⁷J. Wiktor, G. Jomard, and M. Torrent, “Two-component density functional theory within the projector augmented-wave approach: Accurate and self-consistent computations of positron lifetimes and momentum distributions,” *Phys. Rev. B* **92**(12), 125113 (2015).
- ¹⁸A. H. Romero, D. C. Allan, B. Amadon, G. Antonius, T. Applencourt, L. Baguet, J. Bieder, F. Bottin, J. Bouchet, E. Bousquet, F. Bruneval, G. Brunin, D. Caliste, M. Côté, J. Denier, C. Dreyer, P. Ghosez, M. Giantomassi, Y. Gillet,

- O. Gingras, D. R. Hamann, G. Hautier, F. Jollet, G. Jomard, A. Martin, H. P. C. Miranda, F. Naccarato, G. Petretto, N. A. Pike, V. Planes, S. Prokhorenko, T. Rangel, F. Ricci, G.-M. Rignanese, M. Royo, M. Stengel, M. Torrent, M. J. van Setten, B. Van Troeye, M. J. Verstraete, J. Wiktor, J. W. Zwanziger, and X. Gonze, "ABINIT: Overview and focus on selected capabilities," *J. Chem. Phys.* **152**(12), 124102 (2020).
- ¹⁹X. Gonze, B. Amadon, G. Antonius, F. Arnardi, L. Baguet, J.-M. Beuken, J. Bieder, F. Bottin, J. Bouchet, E. Bousquet, N. Brouwer, F. Bruneval, G. Brunin, T. Cavignac, J.-B. Charraud, W. Chen, M. Côté, S. Cottenier, J. Denier, G. Geneste, P. Ghosez, M. Giantomassi, Y. Gillet, O. Gingras, D. R. Hamann, G. Hautier, X. He, N. Helbig, N. Holzwarth, Y. Jia, F. Jollet, W. Lafargue-Dit-Hauret, K. Lejaeghere, M. A. L. Marques, A. Martin, C. Martins, H. P. C. Miranda, F. Naccarato, K. Persson, G. Petretto, V. Planes, Y. Pouillon, S. Prokhorenko, F. Ricci, G.-M. Rignanese, A. H. Romero, M. M. Schmitt, M. Torrent, M. J. van Setten, B. Van Troeye, M. J. Verstraete, G. Zerah, and J. W. Zwanziger, "The Abinit project: Impact, environment and recent developments," *Comput. Phys. Commun.* **248**, 107042 (2020).
- ²⁰F. Linez, I. Makkonen, and F. Tuomisto, "Calculation of positron annihilation characteristics of six main defects in 6H-SiC and the possibility to distinguish them experimentally," *Phys. Rev. B* **94**(1), 014103 (2016).
- ²¹J. Wiktor, G. Jomard, M. Torrent, M.-F. Barthe, and M. Bertolus, "Fully self-consistent calculations of momentum distributions of annihilating electron-positron pairs in SiC," *Phys. Rev. B* **93**(19), 195207 (2016).
- ²²P. E. Blöchl, "Projector augmented-wave method," *Phys. Rev. B* **50**(24), 17953–17979 (1994).
- ²³N. A. W. Holzwarth, A. R. Tackett, and G. E. Matthews, "A projector augmented wave (PAW) code for electronic structure calculations, part I: Atompaw for generating atom-centered functions," *Comput. Phys. Commun.* **135**(3), 329–347 (2001).
- ²⁴I. Makkonen, M. Hakala, and M. J. Puska, "Modeling the momentum distributions of annihilating electron-positron pairs in solids," *Phys. Rev. B* **73**(3), 035103 (2006).
- ²⁵I. Makkonen and F. Tuomisto, "Perspective on defect characterization in semiconductors by positron annihilation spectroscopy," *J. Appl. Phys.* **135**(4), 040901 (2024).
- ²⁶H. Stachowiak, J. Mayersl, and R. N. West, "Selective enhancement of different electron populations by electron-positron attraction: Application to zinc," *J. Phys. F: Met. Phys.* **17**, 1365 (1987).
- ²⁷M. Alatalo, B. Barbiellini, M. Hakala, H. Kauppinen, T. Korhonen, M. J. Puska, K. Saarinen, P. Hautojärvi, and R. M. Nieminen, "Theoretical and experimental study of positron annihilation with core electrons in solids," *Phys. Rev. B* **54**(4), 2397–2409 (1996).
- ²⁸F. Tuomisto and I. Makkonen, "Defect identification in semiconductors with positron annihilation: Experiment and theory," *Rev. Mod. Phys.* **85**(4), 1583–1631 (2013).
- ²⁹J. V. Olsen, P. Kirkegaard, and M. Eldrup, "Analysis of positron lifetime spectra using the PALSfit3 program," *AIP Conf. Proc.* **2182**, 040005 (2019).
- ³⁰J. Wiktor, G. Jomard, M. Torrent, and M. Bertolus, "Electronic structure investigation of energetics and positron lifetimes of fully relaxed monovacancies with various charge states in 3C-SiC and 6H-SiC," *Phys. Rev. B* **87**(23), 235207 (2013).
- ³¹J. Wiktor, X. Kerbiriou, G. Jomard, S. Esnouf, M.-F. Barthe, and M. Bertolus, "Positron annihilation spectroscopy investigation of vacancy clusters in silicon carbide: Combining experiments and electronic structure calculations," *Phys. Rev. B* **89**(15), 155203 (2014).
- ³²J. F. Ziegler, M. D. Ziegler, and J. P. Biersack, "SRIM – The stopping and range of ions in matter (2010)," *Nucl. Instrum. Methods Phys. Res. Sec. B* **268**(11–12), 1818–1823 (2010).